bioRxiv preprint doi: https://doi.org/10.1101/464438; this version posted November 7, 2018. The copyright holder for this preprint (which was not certified by peer review) is the author/funder. All rights reserved. No reuse allowed without permission.

Concurrent EEG- and fMRI-derived functional connectomes exhibit linked dynamics

Jonathan Wirsich[1,2], Anne-Lise Giraud[3], Sepideh Sadaghiani[1,2]

[1]Beckman Institute for Advanced Science and Technology, University of Illinois at Urbana-Champaign, Urbana, IL, USA
[2]Department of Psychology, University of Illinois at Urbana-Champaign, Urbana, IL, USA
[3]Department of Neurosciences, University of Geneva, Geneva, Switzerland

Large-scale functional connectivity of the human brain, commonly observed using functional Magnetic Resonance Imaging (fMRI), exhibits a whole-brain spatial organization termed the functional connectome. The fMRI-derived connectome shows dynamic reconfigurations that are behaviorally relevant. Due to the indirect nature of fMRI, it is unclear whether such topographic changes reliably reflect modulation in neuronal connectivity patterns. Here, we directly compared concurrent fMRI-derived and electrophysiological connectivity dynamics on a connection-wise basis across the whole connectome.

Dynamic whole-brain functional connectivity (dFC) was assessed during resting-state in two independent concurrent fMRI-electroencephalography (EEG) datasets (42 subjects total) using a sliding window approach. FMRI- and EEG-derived dFC shared significant mutual information in all canonical EEG frequency bands. Notably, this was true for virtually all connections. Across all EEG frequency bands, connections with the strongest link between EEG and fMRI dynamics tied the default mode network (DMN) to the rest of the brain. Beyond this frequency-independent multimodal dFC, fMRI connectivity covaried with EEG connectivity in a frequency-specific manner in two distributed sets of connections for delta and gamma bands, respectively. These results generalized across the two datasets.

Our findings promote the DMN as a universal hub of dynamics across frequencies, but also show that spatial distribution of fMRI and EEG dFC differ across the canonical EEG-frequency bands. This study reveals a close relationship between time-varying changes in whole-brain connectivity patterns of electrophysiological and hemodynamic signals. The results support the value of EEG for studying the whole-brain connectome and provide evidence for a neuronal basis of fMRI-derived dFC.

Introduction

To date, our knowledge about the topography of neural communication in the human brain is largely derived from fMRI, an indirect measure of neural activity. Since the discovery that brain activity is correlated between distant brain regions in resting-state functional magnetic resonance imaging (rs-fMRI) (1) extensive efforts have been undertaken towards establishing the neural origin of this functional connectivity (FC) (2–8). Using fMRI, the brain has been characterized in terms of different intrinsic connectivity networks (ICNs) (9–11). Collectively, the connectivity within and between ICNs can be represented as a whole-brain connectivity graph, or connectome(12). This line of research has traditionally focused on static properties of FC by averaging brain activity across the entire recording period (13). Though dominated by fMRI-based research, *static* whole-brain FC has been shown to have a spatial organization comparable across EEG and fMRI (2, 5) and MEG and fMRI (4, 6) and intracranial EEG.

bioRxiv preprint doi: https://doi.org/10.1101/464438; this version posted November 7, 2018. The copyright holder for this preprint (which was not certified by peer review) is the author/funder. All rights reserved. No reuse allowed without permission.

More recently, the static view on FC has been extended by looking into the dynamic FC changes (dFC) of rs-fMRI connectivity in time windows of seconds to minutes (14, 15). Such dynamics have been shown to switch between recurrent metastates (16, 17). Additionally, fMRI-derived dynamics correlate with behavior (18–20), and are clinically relevant for identifying aberrant dynamic brain state changes (for review see (21)). However, it is still unclear how reliably dFC derived from fMRI can measure neuronal dynamics (22). Investigations of time-varying fMRI connectivity have been plagued by concerns about physiological noise, head motion, and sampling variability (23, 24), and important discussions about optimal null models to account for such spurious 'dynamics' are currently ongoing (15, 22).

On the other hand, dynamic modulation in phase synchrony of neurophysiological oscillations as measured by EEG and MEG has been well-established as a mechanism for long-range neural communication (25, 26). However, it is unknown whether these neurophysiological connectivity dynamics extend to infraslow time scales comparable to those driving dFC in fMRI (dominated by <0.1Hz range). Indications that this may be the case come from studies assessing phase synchrony at sensor level and building a coarse global field average across EEG electrode pairs (27, 28), but electrophysiological investigations in spatially resolved connectomes are missing to date. While neurophysiological measures are subject to limitations such as limited spatial localizability of scalp recordings, recent methodological advances have made it possible to establish whole-brain connectivity patterns and their dynamics from source-localized signals, at least for coarse whole-brain parcellations (29, 30). Applying these methodological advances, source-localized MEG-based connectivity studies have reported time-varying interregional connectivity at fast time scales (31, 32). However, as MEG and fMRI cannot be recorded concurrently, it remains unclear whether dynamics in the MEG-derived connectome coincide with those observed in fMRI-derived dFC. Consequently, the relationship of connectivity dynamics across neurophysiological and hemodynamic connectomes is unknown.

Concurrent recordings of hemodynamic and neurophysiological signals help investigate 1.) the neural origin of fMRI-derived dFC, and 2.) whether fast neurophysiological signals exhibit slow dynamics that concurrently follow the same spatial pattern as that of fMRI. Global neurophysiological measures such as EEG band-limited global field power have been linked to fMRI-based dFC both in specific intrinsic networks (33) and the whole brain (34). Allen et al. (35) demonstrated that the reoccurring states in fMRI-based dFC are related to concurrent states of the EEG power spectrum. Though the correlation between global measures of EEG activity and local fMRI-FC in both human and animal research is suggestive of the neuronal basis of dFC (36, 37), previous work still lacks the demonstration that dFC is locally related across modalities on a connection-wise basis. Using concurrent intracranial-EEG and fMRI in presurgical patients, we previously observed a significant correlation between the dynamic sliding window variance of intracranial-EEG connectivity and BOLD connectivity (38). However, it remains unclear if this variance correlation reflects a true relationship between the EEG and BOLD connectivity timecourses on a whole-brain level.

Here, we hypothesize that dFC derived from source-space EEG covaries over time with fMRI dFC on a connection-wise basis across the whole brain. Further, we aimed to characterize the whole-brain topological organization of this cross-modal relationship for each canonical EEG frequency band.

bioRxiv preprint doi: https://doi.org/10.1101/464438; this version posted November 7, 2018. The copyright holder for this preprint (which was not certified by peer review) is the author/funder. All rights reserved. No reuse allowed without permission.

Results

Static connectivity relationship across EEG and fMRI

We used resting-state concurrent EEG-fMRI data from two independent datasets (primary n=26, generalization n=16). Preprocessed fMRI signal was averaged to the 68 cortical regions of the Desikan atlas (39, 40). Preprocessed EEG signals band-passed to each canonical frequency band (δ,θ,α,β,γ) were source-reconstructed (41–43) to the same atlas (Fig. 1a). First, we sought to confirm that the previously reported static relation between fMRI-derived and EEG-derived connection-wise connectivity strength (3, 8) holds true for the two datasets of this study. To this end, we assessed connectivity averaged across the total duration of EEG and fMRI data. Connectivity in source-projected EEG was quantified as band-limited phase synchrony using imaginary coherence, and connectivity in fMRI was quantified as Pearson's r for the same whole-brain parcellation atlas. In line with our prior work (8), static FC averaged of all EEG bands were correlated to FC of fMRI (main dataset fMRI vs. δ/θ/α/β/γ: r=0.34/0.34/0.33/0.36/0.29; generalization dataset fMRI vs. δ/θ/α/β/γ: r=0.34/0.33/0.36/0.41/0.39, taking the average FC across all subjects). This observation reaffirms the link between the spatial organization of connectivity across modalities and confirms sufficient quality of EEG source localization to the whole-brain parcellation.

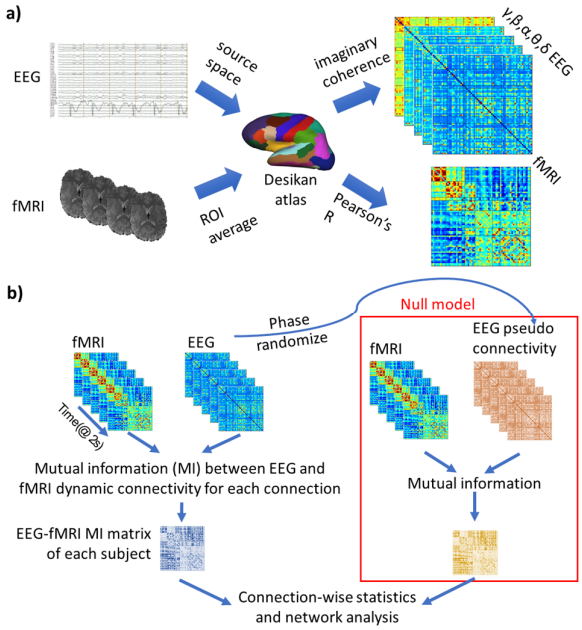

Fig. 1: a) Construction of EEG and fMRI connectomes. EEG was source reconstructed and fMRI signal was averaged for the 68 cortical regions of the Desikan atlas (39). Pearson's correlation of fMRI timecourses and imaginary coherence of band-limited EEG source signal were used to build connectomes. b) Dynamic FC was derived from a 1min window sliding at 2s (= repetition time of fMRI). Mutual information between fMRI-dFC and EEG-dFC was statistically compared to a null model consisting of the mutual information between fMRI-dFC and phase scrambled EEG-dFC *(8, 44)*.

Dynamic connectivity relationship across EEG and fMRI

Next, we used a sliding window approach to assess whether time-varying changes in the whole-brain connectivity pattern derived from fMRI are linked to dynamics in band-limited phase synchrony across modalities (Fig. 1b). We used the information-theoretic measure of mutual information, which assesses the relationship between the modalities without assuming linearity. We tested these co-dynamics against a null model that spatially randomizes connections of the EEG connectome while preserving comparable modular organization (8, 44). Dynamic FC in δ, θ, α, β and γEEG showed high mutual information with fMRI connectome dynamics significantly outperforming the null model in

bioRxiv preprint doi: https://doi.org/10.1101/464438; this version posted November 7, 2018. The copyright holder for this preprint (which was not certified by peer review) is the author/funder. All rights reserved. No reuse allowed without permission.

virtually all region-pairs: in 100% of connections for fMRI vs. δEEG-fMRI, θEEG-fMRI, αEEG-fRMI, and γEEG-fMRI, and in 99.91% of connections for βEEG-fMRI (Bonferroni corrected for 2248 connections, $p<2.19*10^{-5}$). This strong cross-modal relationship was confirmed in the generalization dataset, although it was significant in a smaller number of connections especially for βEEG-fMRI and γEEG-fMRI: fMRI vs. δEEG-fMRI=98.68%, θEEG-fMRI=91.83% αEEG-fRMI=87.97%, βEEG-fMRI=54.48%, γEEG-fMRI=31.12% (Bonferroni corrected for 2248 connections, $p<2.19*10^{-5}$). The relative reduction in effect size in the replication dataset is in line with the smaller sample size and shorter recording duration. Fig. 2 show the distribution of mutual information of one randomly selected subject per dataset.

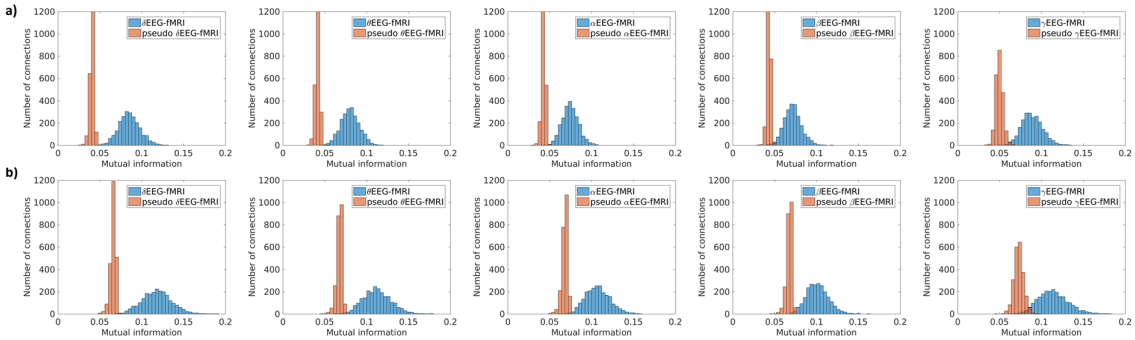

Fig. 2: Distribution of mutual information between fMRI and EEG dFC time courses using real EEG and phase-scrambled EEG (null model) across all bands. Data are shown for a randomly selected subject of a) the main dataset and b) the generalization dataset. Note that the null model maintains (and thus controls for) the individual subject's global mean shifts that may result from time-varying noise sources that broadly affect connectivity in both EEG and fMRI. For virtually all connections of the main dataset, EEG and fMRI dynamics are significantly linked over time irrespective of EEG oscillation band. A similar effect is observed for the vast majority of connections in the generalization dataset.

Additionally, we tested for generalizability at a connection-wise level. The connection-wise strength of mutual information averaged across all subjects was strongly correlated across primary and replication datasets for fMRI compared to δ/θ/αEEG (r=0.48/0.46/0.34) although no correlation was observed for fMRI vs. β/γEEG (r=0.04/-0.02, Fig. 3). A split-half approach indicated that the lack of connection-wise generalization for β and γ bands is due to the lower signal-to-noise ratio compared with the slower frequencies (SI Results and Table S1).

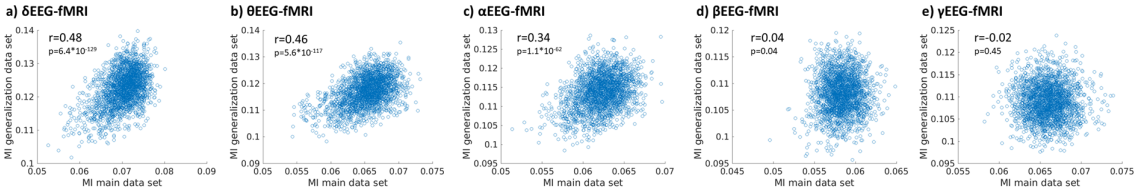

Fig. 3: Connection-wise comparison of the EEG-fMRI relationship across the two datasets. Each data point reflects the mutual information between EEG-dFC and fMRI-dFC for a given connection averaged across all subjects of the respective datasets. Scatter plots are provided for the relation of fMRI-dFC to a) δEEG, b) θEEG, c) αEEG, d) βEEG, and e) γEEG-dFC. The whole-brain distribution of mutual information correlated across the two datasets for δ, θ and αEEG.

In summary, fMRI signal correlations were linked to slow modulations of oscillatory phase synchrony across the vast majority of the connectome's region-pairs. This was true for all canonical EEG frequency bands across both datasets. The strength of the EEG-fMRI relationship was correlated on a connection-wise basis between primary and generalization datasets in the δ, θ, and α bands.

bioRxiv preprint doi: https://doi.org/10.1101/464438; this version posted November 7, 2018. The copyright holder for this preprint (which was not certified by peer review) is the author/funder. All rights reserved. No reuse allowed without permission.

Spatial topography of the dynamic relationship

Next, we sought to characterize the spatial topography of co-dynamics beyond the above-described all-encompassing relation between EEG and fMRI dFC. Specifically, we assessed how the connections for which fMRI dFC was *most strongly* linked to EEG dFC were distributed over canonical neurocognitive ICNs (11) and across EEG frequency bands. To this end, the contrast of EEG-fMRI mutual information in real against null data was subjected to network based statistics (NBS) (45) separately for each EEG frequency band. The initial element-wise t-threshold was chosen so that NBS would identify the connected set of 200 connections with strongest mutual information between EEG and fMRI dynamics. The connection-wise threshold and the ensuing NBS cluster-corrected significance corresponding to the top-200 cutoff are listed in Table 1. For both datasets the top 200 connections are consistently drawn from connections that have high mutual information (see SI Results).

Table 1: Statistical comparison (NBS, 5000 iterations) of mutual information between EEG- and fMRI-derived dFC against mutual information from the null model. The t-threshold (one-sided) was chosen to identify the connected set of 200 connections with strongest EEG-fMRI relationship. The ensuing top 200 connections are visualized in Fig. 4.

Main dataset	**T**	**P (NBS-corrected)**
δEEG-fMRI vs. δEEG-fMRI Null	9.133	<0.0002
θEEG-fMRI vs. θEEG-fMRI Null	8.056	<0.0002
αEEG-fMRI vs. αEEG-fMRI Null	7.411	<0.0002
βEEG-fMRI vs. βEEG-fMRI Null	6.243	<0.0002
γEEG-fMRI vs. γEEG-fMRI Null	5.715	<0.0002
Generalization dataset		
δEEG-fMRI vs. Null	9.605	<0.0002
θEEG-fMRI vs. θEEG-fMRI Null	8.265	<0.0002
αEEG-fMRI vs. αEEG-fMRI Null	7.443	<0.0002
βEEG-fMRI vs. βEEG-fMRI Null	6.646	<0.0002
γEEG-fMRI vs. γEEG-fMRI Null	7.157	<0.0002

Fig. 4 visualizes the networks of the respective top-200 connections linked between fMRI dFC and EEG dFC for each canonical oscillation band. To understand the distribution of the top 200 connections with respect to ICNs, we mapped the connections to an atlas of seven canonical networks ((11), Fig 4a). The number of connections between any given pair of canonical networks is visualized in Fig 4b. This distribution of pairwise network connection density was strongly correlated across primary and generalization datasets for all bands (δ/θ/α/β/γ: r=0.82/0.83/0.93/0.85/0.85). To test if the top-200 connections were distributed across the canonical ICNs in a similar fashion for both datasets we randomly permuted the top-200 connections in both datasets. We observed no significant difference between datasets in this permutation analysis (n=100,000 iterations, p>0.0018 for all EEG frequency bands, Bonferroni corrected for multiple comparisons at 28 network pairs). Thus, while we observed connection-wise generalization for δ/θ/α but not β/γ bands (Fig. 3), the results in Fig. 4 support generalization for all bands at the coarser ICN-wise resolution.

bioRxiv preprint doi: https://doi.org/10.1101/464438; this version posted November 7, 2018. The copyright holder for this preprint (which was not certified by peer review) is the author/funder. All rights reserved. No reuse allowed without permission.

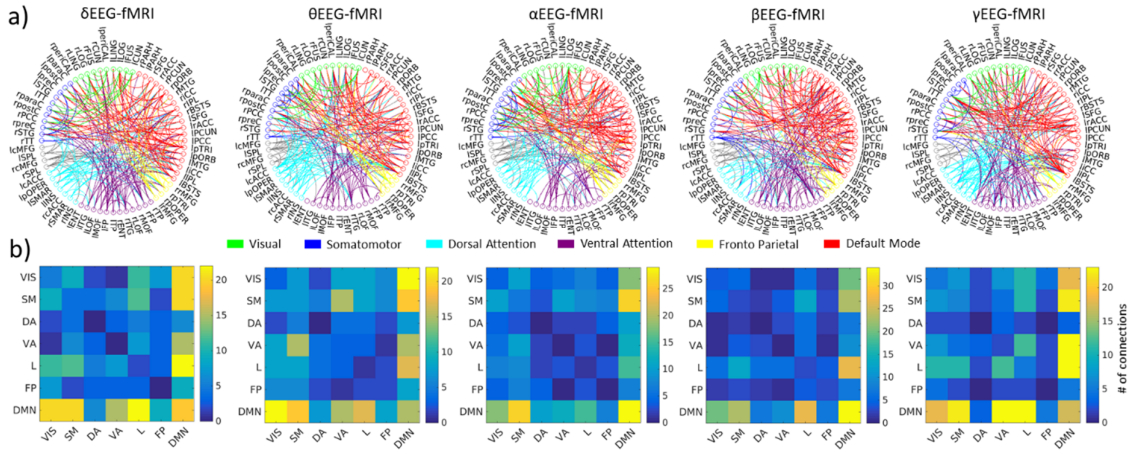

Fig. 4: Spatial characterization of linked EEG-fMRI connectivity dynamics. a) Topographical distribution of the 200 connections with the strongest EEG-fMRI relationship (determined by NBS, 5000 iterations, cf. Table 1). Connections are color-coded according to the seven major canonical intrinsic networks (11). Individual region labels are listed in table S7. b) Mapping of those 200 connections to the intrinsic networks. The color scale depicts the count of connections falling between a given pair of canonical intrinsic networks. For all EEG frequency bands, the top 200 connections are dominated by within- and between-network connections of the DMN. Results are visualized for the primary dataset, while a strongly correlated distribution over intrinsic networks was observed in the generalization dataset (Tables S2-S6).

Interestingly, for all EEG frequencies, this distributed network of strongest cross-modal dynamics aligned with the Default Mode Network (DMN). We established that this distribution of the top 200 connections and the ensuing DMN-dominance were not driven by the number of ICN nodes or other potential biases. For each network pair (e.g. DMN-VIS) we tested whether the number of connections was significantly higher than chance by randomly selecting (n=100,000) 200 connections from the main dataset (Tables S2-S6). Additional frequency-specific connections were observed beyond DMN-dependent connectivity, most notably for δ: FP-VIS; θ: VA-SM, FP-VS; α: SM-VA, β: FP-F, and γ: VA-L (Fig. 4b, Tables S2-S6).

In summary, while our first analysis showed a widespread significant relationship between fMRI and EEG for virtually all connections and irrespective of oscillation frequency, the connections of the *strongest* (top 200) cross-modal relationship showed a dominant role of the DMN.

Frequency-specificity of the dynamic relationship

Finally, we sought to directly and statistically corroborate the frequency specificity of the cross-modal relationship on a connection-wise basis. To this end, we combined the EEG-fMRI mutual information matrices for all EEG bands into an ANOVA (5 levels for 5 frequency bands). Statistical testing indicated a main effect of EEG band (F-test, p=0.041, NBS corrected). Exploratory post-hoc t-tests revealed that both delta- and gamma-band dFC are organized in a frequency specific network of increased mutual information to fMRI dynamics relative to all other frequencies ($p<0.05$, NBS-corrected, Table 2). Fig. 5a visualizes this frequency-specific network for delta and gamma bands in physical brain space, and Fig. 5b maps the connections according to canonical ICNs (we report the connected set of top 100 connections). Confirming the observation described above (Fig. 4b), both networks of frequency specific cross-modal dynamics consisted predominantly of DMN connections to the rest of the brain; the delta-specific set showed a strong preference for Limbic-DMN connections whereas the gamma specific set shared a preference between DMN-Ventral-attention and DMN-Limbic connections (Fig. 5c).

bioRxiv preprint doi: https://doi.org/10.1101/464438; this version posted November 7, 2018. The copyright holder for this preprint (which was not certified by peer review) is the author/funder. All rights reserved. No reuse allowed without permission.

Table 2: Table 2: NBS (5000 iterations) shows a network of significantly increased mutual information for δEEG-fMRI and γEEG-fMRI (connection-wise T-threshold is chosen to limit the network size to 100 connections, one sided t-test one band to all the others). The ensuing top 100 connections are visualized in Fig. 5.

Main dataset	**T**	**P (NBS-corrected)**
δEEG-fMRI > All other bands	1.867	0.024
γEEG-fMRI > All other bands	1.875	0.023
Generalization dataset		
δEEG-fMRI > All other bands	2.27	0.006
βEEG-fMRI > All other bands	2.375	<0.0002
γEEG-fMRI > All other bands	2.075	0.0162

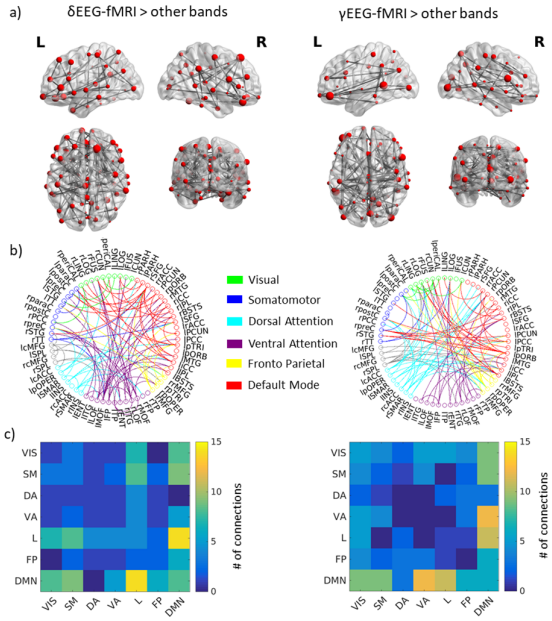

Fig. 5: Frequency-specificity of linked EEG-fMRI connectivity dynamics. a) Topographical distribution of the top-100 connections in which connectivity dynamics were more strongly linked between fMRI and δEEG than other EEG bands (left) and between fMRI and γEEG compared to other bands (determined by NBS, 5000 iterations, cf. table 2). Color code and region labels correspond to Fig. 4. b) The count of connections among the top 100 falling between a given pair of canonical intrinsic networks. The δ-dominated set of connections tie the DMN to the Limbic network, whereas the γ-dominated set of connections predominantly tie the DMN to the Ventral Attention and Limbic networks. Results are visualized for the primary dataset, while spatial specificity for δ and γ bands was likewise observed in the generalization dataset (table 2).

In the generalization dataset the F-test and NBS analysis likewise showed a significant main effect of frequency (F<0.0002). Exploratory post-hoc analysis replicated a set of connections with significantly higher mutual information for δEEG-fMRI and γEEG-fMRI, and additionally for βEEG-fMRI (Table 2). To conclude, when contrasted directly across frequency bands, frequency-specificity of the EEG-fMRI relationship was confirmed with a DMN dominance.

bioRxiv preprint doi: https://doi.org/10.1101/464438; this version posted November 7, 2018. The copyright holder for this preprint (which was not certified by peer review) is the author/funder. All rights reserved. No reuse allowed without permission.

Discussion

Dynamics of intrinsic brain activity are necessary for human behavior, which is inherently flexible. While these dynamics are most commonly studied using fMRI, the relationship between BOLD dynamics and their underlying neurophysiological basis is still unclear. In this study, we demonstrated that dFC derived from fMRI shares mutual information with EEG-derived dFC in all canonical frequency bands. Importantly, this applies to the whole connectome. Further, the relative contribution of each EEG frequency band to BOLD connectivity dynamics varies across space. These results shed new light on the relationship between electrophysiological and BOLD connectivity dynamics and in particular provide strong evidence that BOLD-derived dFC is directly linked to neurophysiological dynamics with corresponding spatial organization.

Static connectivity

In line with prior work, the spatial pattern of static EEG and fMRI connectomes were significantly correlated. Only two prior studies have investigated whole-brain connectomes in concurrent EEG and fMRI (3, 8), and the current study confirms this important observation. However, the two prior studies were restricted to static relationships, while the true advantage of concurrent as opposed to separately recorded EEG and fMRI connectivity lies in its potential to reveal dynamics co-fluctuating across modalities.

Dynamic connectivity

Dynamic FC has been shown to exist both on slow hemodynamic (14) and fast electrophysiological timescales (31, 32). Regarding the relationship between EEG and fMRI, Chang et al. (33) and Allen et al. (35) showed that BOLD FC dynamics are linked to band-limited EEG global field power. The current study advances to spatially resolved EEG connectomes, demonstrating the link between slow dynamics of fast electrophysiological connectivity and the slow BOLD connectivity dynamics.

This finding has implications for the interpretation of fMRI-derived dFC. Since physiological and non-physiological noise heavily contribute to fMRI-derived dFC, the degree to which such dynamics reflect changes in neural communication is difficult to assess; choosing an appropriate null model can be challenging (15, 22). Instead of comparing fMRI dFC to a null model, we chose to compare fMRI dynamics to direct measures of neural dynamics such as MEG or EEG. Our approach of concurrently assessing dFC in EEG provides evidence that veridic dynamics can indeed be derived from fMRI, as they are directly related to slow changes in the underlying electrophysiological connectivity. Another important advantage of our approach is the independence of outcomes from both EEG- and fMRI-related artefacts (e.g. eye movements in EEG or magnetic field inhomogeneities in fMRI), since spurious dynamics due to random noise in each modality will cancel each other out in the joint model we utilized. Comparing a global EEG parameter to local fMRI connections is an approach prone to spurious cross-modal links stimming from a connection-unspecific global shift (e.g. breathing(46)). In contrast, our approach comparing both modalities on a connection-wise level is unlikely to be impacted by averaged global patterns.

Our results also have important implications for neurophysiological connectivity dynamics with respect to methodological reliability and observed timescales. Due to concerns regarding the ill-posed nature of EEG source localization, connectivity approaches in whole-brain parcellation space are underused (30). The close connection-wise relationship to fMRI-derived dFC provides strong support for the relevance of source-localized EEG to the study of the whole-brain functional connectome. With respect to timescales, prior MEG-based whole-brain investigations have established fast dynamics in interregional connectivity at ~50-100ms (31, 32). Connectivity dynamics at these fast timescales in EEG have been shown to correlate with the slow changes observed in fMRI, albeit in EEG sensor space

bioRxiv preprint doi: https://doi.org/10.1101/464438; this version posted November 7, 2018. The copyright holder for this preprint (which was not certified by peer review) is the author/funder. All rights reserved. No reuse allowed without permission.

rather that reconstructed brain parcellations (47, 48). Concurrent EEG-fMRI studies investigating neurophysiological dynamics at *infraslow* speeds (typically defined as < 0.1Hz (49, 50)) have been either limited to a coarse global field average of connectivity across EEG electrode pairs (27, 28), or have focused solely on signal fluctuations (Hiltunen et al. (49)). Extending beyond these important studies, we show that connectivity derived from fast oscillation phase synchrony in EEG exhibits meaningful fluctuations in the infraslow range.

Spatial distribution of the cross-modal dynamics

We found the strongest relationship between EEG and fMRI dynamics in cortico-DMN connections. The dominance of DMN interactions with other ICNs has been previously demonstrated for dynamic connectivity derived from MEG (51). Similarly, Vidaurre et al. (32) observed increased MEG within-network coherence in the DMN as opposed to visual and sensorimotor areas. More generally, the DMN has been proposed to form a central hub that integrates multisensory input from different brain regions (52). As such, it is no surprise that we observed connections between DMN and the visual and motor systems to show some of the strongest relations between EEG and fMRI.

Interestingly, connections with the strongest interrelation between EEG and fMRI connectivity predominantly spanned the canonical intrinsic networks. While we found that the vast majority of connections were dynamically linked between EEG and fMRI, the cross-modal relation was weaker within as compared to across networks with the exception of DMN-DMN connectivity. This finding may seem counterintuitive since the investigation of amplitude fluctuations (as opposed to connectivity) shows a strong link between EEG and fMRI within ICNs (53, 54), suggesting a strong static within-network connectivity. Similarly, de Pasquale et al. (51) observed strong within-network connectivity dynamics for αand βbands alongside between-network connectivity dynamics. One possible explanation for our results is that within-network connections are less dynamic than connections between different intrinsic networks. This is in line with the observation that DMN regions are among the most dynamic, as measured by fMRI-derived dFC (15).

Frequency specificity of the cross-modal dynamics

We observed both a delta dominance in DMN-limbic connections and γ-dominance in VA-DMN connections (Fig. 4). The relationship between *static* MEG and fMRI connectivity has been shown to vary across connections depending on neurophysiological frequency (5). Likewise, spatially distinct patterns of frequency-specific connectivity *dynamics* have been observed in MEG (32). As such, Vidaurre et al. (32) have suggested a division of the DMN into a low-frequency and a high-frequency subnetwork. Although the network subdivisions used by Vidaurre et al. (32) do not directly map to the spatial distribution of the canonical ICN networks that we chose, our results for delta vs. γ-are in line with a low and high frequency-specific contribution of connections encompassing the DMN. This suggests a differential organization of frequencies in the DMN, which are synced between EEG and fMRI dynamics.

Methodological considerations and limitations

The relatively low spatial resolution (number of regions) of the selected Desikan atlas was imposed by the number of 64 EEG electrodes. While it has been shown that a parcellation adapted to the actual EEG montage improves the quality of the source reconstruction (55), it is unclear if the fMRI signal would suffer from a parcellation scheme imposed by the EEG montage. A future approach could be extending the MR-compatible EEG setup to 128 or 256 electrodes (56) to gain data quality comparable to MEG recordings (57). Regarding temporal resolution, the sliding window approach has been previously criticized for assuming slowly changing dynamics as opposed to fast instantaneous switches (see (21) for review). While the timescale of observable dynamics depends on the choice of window

bioRxiv preprint doi: https://doi.org/10.1101/464438; this version posted November 7, 2018. The copyright holder for this preprint (which was not certified by peer review) is the author/funder. All rights reserved. No reuse allowed without permission.

length, a comparative analysis of the optimal windowing parameters to derive dFC was beyond the scope of this study. Importantly, we show that results from the chosen parameter set generalize across two independent datasets.

Our focus on common patterns generalizing across datasets resulted in a stringent statistical threshold (cf. Table 1) that comes at the cost of being insensitive to small effects. This was primarily a result of the limited power of the generalization dataset (smaller sample size and shorter recordings). In particular, β-and γ-connectivity seem to be influenced by the low signal-to-noise ratio of the generalization dataset (with 45.52% and 68.88% of βEEG- and γEEG-derived connections sharing no significant dynamics with fMRI, as opposed to virtually no insignificant connections in the primary dataset). Beyond the signal-to-noise limitations in human concurrent EEG-fMRI, there is evidence that γ-and β-band connectivity may contain information complementary to fMRI-derived connectivity. A weaker relation to fMRI connectivity has been reported for β and low-γ compared to other bands in intracranial electrophysiological recordings in humans (38, 58) and in animals (59, 60). The weaker relationship for β-and low γ-bands likely reflects a general property of the electrophysiology-fMRI relationship. This interpretation is also in line with our previous finding that γ-connectivity shows a unique relationship to structural connectivity not shared by fMRI-derived connectivity (8). Importantly, at the coarser ICN-wise (Fig. 4) as compared to connection-wise resolution (Fig. 3), the results generalized across all bands including β and γ. The generalization of effects in this study is especially supportive of the robustness of the EEG-fMRI dFC relationship in light of substantial differences across the two datasets (3T vs. 1.5T MRI field strength, eyes-closed vs. eyes-open resting-state and differences in fMRI sequences and subject demographics).

Conclusion

We observed a link between electrophysiological and fMRI-derived dynamic functional connectivity which demonstrates, on a connection-wise level across the whole brain, that fMRI-derived connectivity entails slow dynamics of fast electrophysiological connectivity. While this link exists across all canonical electrophysiological frequency bands, the strength of the cross-modal relationship varies over connections in a frequency-specific manner, especially for δ-and γ-bands. In conclusion, this study provides strong multimodal evidence of slow time varying connectivity dynamics of intrinsic brain activity.

bioRxiv preprint doi: https://doi.org/10.1101/464438; this version posted November 7, 2018. The copyright holder for this preprint (which was not certified by peer review) is the author/funder. All rights reserved. No reuse allowed without permission.

Methods

We analyzed a primary dataset (n=26) and tested for generalizability across a different sample by using an independent dataset (n=16) from a different site. The generalization dataset is openly available at https://osf.io/94c5t/ and described in detail in Deligianni et al. (3, 61).

Primary Dataset

Subjects

We recruited 26 healthy subjects (8 females, mean age 24.39, age range 18-31) with no history of neurological or psychiatric illness. Ethical approval has been obtained from the local Research Ethics Committee (CPP Ile de France III) and informed consent has been obtained from all subjects.

Data Acquisition

We acquired three runs of 10 minutes eyes-closed resting-state in one concurrent EEG-fMRI session (Tim-Trio 3T, Siemens). FMRI parameters comprised 40 slices, TR=2.0s, 3.0x3.0x3.0mm, TE = 50ms, field of view 192, FA=78°. EEG was acquired using an MR-compatible amplifier (BrainAmp MR, sampling rate 5kHz), 62 electrodes (Easycap), referenced to FCz, 1 ECG electrode, and 1 EOG electrode. Scanner clock was time-locked with the amplifier clock (62). Additionally, an anatomical T1-weighted MPRAGE sequence was acquired (176 slices, 1.0x1.0x1.0 mm, field of view 256, TR=7min).

The acquisition was part of a study with two additional naturalistic film stimulus of 10 minutes not analyzed in the current study, and acquired after runs 1 and 2 of the resting state as described in Morillon et al. (63). The three runs resulted in a total length of 30 minutes of resting-state fMRI per subject. Subjects wore earplugs to attenuate scanner noise and were asked to stay awake, avoid movement and close their eyes during resting-state recordings. In three subjects, one of three rest sessions each was excluded due to insufficient EEG quality.

Data processing

Atlas

T1-weighted images were used to delineate 68 cortical regions of the Desikan atlas (39, 40) and to extract a gray matter mask (recon-all, Freesurfer suite v6.0.0, http://surfer.nmr.mgh.harvard.edu/).

fMRI

The BOLD timeseries were corrected for slice timing and spatially realigned using the SPM12 toolbox (revision 6906, http://www.fil.ion.ucl.ac.uk/spm/software/spm12). Mean white matter and cerebrospinal fluid timecourses were extracted from a manually defined spherical 5mm ROIs using MarsBaR (v0.44, http://marsbar.sourceforge.net/). Using the FSL toolbox (v5.0, https://fsl.fmrib.ox.ac.uk/fsl/) the scull-stripped T1 image (fsl-bet), Desikan atlas, and grey matter delineation were linearly coregistered into the subject space of the T2* images (fsl-flirt v6.0). The fMRI timeseries were averaged for each of the 68 atlas regions, and the six movement parameters (from realignment), CSF, white matter and grey matter global signal were regressed out of the region-wise timeseries. The resulting timeseries were bandpass-filtered at 0.009-0.08 Hz (64).

EEG

EEG was corrected for the gradient artefact induced by the scanner using the template subtraction and adaptive noise cancelation followed by lowpass filtering at 75Hz, downsampling to 250Hz (65) and cardiobalistic artefact template subtraction (66) using EEGlab v.7 (http://sccn.ucsd.edu/eeglab) and the FMRIB plug-in (https://fsl.fmrib.ox.ac.uk/eeglab/fmribplugin/). Data then was analyzed with Brainstorm software (43), which is documented and freely available under the GNU general public license (http://neuroimage.usc.edu/brainstorm, version 10th August 2017). Bandpass-filtering was

bioRxiv preprint doi: https://doi.org/10.1101/464438; this version posted November 7, 2018. The copyright holder for this preprint (which was not certified by peer review) is the author/funder. All rights reserved. No reuse allowed without permission.

carried out at 0.3-70 Hz. Data was segmented according to TR of the fMRI acquisition (2s epochs). Epochs containing head motion artifacts in EEG were visually identified after semi-automatically preselecting epochs where signal in any channel exceeded the mean channel timecourse by 4 std. These segments were excluded from the analysis. Electrode positions and T1 were coregistered by manually moving the electrode positions onto the electrode artifacts visible in the T1 image. Using the OpenMEEG BEM model, a forward model of the skull was calculated based on the individual T1 image of each subject (42, 67).

The EEG signal was projected into source space using the Tikhonov-regularized minimum norm (41) with the Tikhonov parameter set to 10% (brainstorm 2016 implementation, assumed SNR ratio 3.0, using current density maps, constrained sources normal to cortex, depth weighting 0.5/max amount 10). Source activity was averaged to the regions of the Desikan atlas. For each epoch (length 2s) imaginary coherence of the source activity was calculated between each regions pair (68) at 2Hz frequency resolution. The 2Hz bins were averaged for 5 canonical frequency bands: delta (0.5-4Hz), theta (4-8Hz), alpha (8-12Hz), beta (12-30Hz), gamma (30-60Hz).

Joint motion scrubbing

For all analyses, both fMRI volumes and EEG epochs were excluded for time periods where motion was identified in either modality. Time periods with motion were defined as volumes exceeding the framewise displacement threshold FD=0.5 in fMRI (69), and by visual inspection in EEG as described above. Additionally, for sliding window connectivity (see section Sliding window connectivity below), windows with more than 10% of their datapoints (>3 fMRI volumes or >3 EEG epochs) removed by this motion scrubbing procedure were excluded from dynamic connectivity analysis. The joint motion scrubbing approach resulted in a mean of 544 out of 870 sliding windows (range 262-813) for the main dataset and 216 out of 272 sliding windows (range 112-259) for the generalization dataset.

Connectivity

Static connectivity

Static connectivity was estimated for fMRI data by calculating Pearson's correlation of the BOLD timecourse between each region pair over the duration of each run and averaged across the 3 runs. For EEG, the connectivity (imaginary coherence) calculated for each 2s epoch was averaged across all runs (Fig. 1a).

Sliding window connectivity

dFC matrices were calculated using a rectangular sliding window of 1 min (using imaginary coherence for EEG and Pearson's correlation for fMRI, this resulted in 30 datapoints per window). The window length was chosen as a tradeoff between maximizing the number of datapoints without discarding relevant dynamic BOLD frequencies (19, 64, 70) while also taking into account the theoretical limitations of shorter window lengths to reliably detect dFC (24, 71). Most importantly we show that the chosen parameter set reliably replicated across two independent datasets.

Normalized mutual information defined by $Y(M;N) = \frac{H(M)+H(N)}{H(M,N)}$ with H(M), H(N) being the entropies of observations N and M and H(M,N) the joint entropy (72, 73) was calculated for the resulting EEG and fMRI dFC matrices, building a new connectivity matrix of joint EEG-fMRI, based on mutual information strength between the modalities (for each EEG frequency band). In contrast to linear measures such as correlation, mutual information is an information theoretic measure which is able to also capture cross-modal relationships in connectivity dynamics without assuming linearity or Gaussian constraints (74). Mutual information has previously been shown to be helpful when combining EEG and fMRI (75).

bioRxiv preprint doi: https://doi.org/10.1101/464438; this version posted November 7, 2018. The copyright holder for this preprint (which was not certified by peer review) is the author/funder. All rights reserved. No reuse allowed without permission.

Null model

For each connection, mutual information was then compared to a null model of EEG-fMRI mutual information using spatially phase-randomized EEG matrices (8, 44). In brief, we applied the approach of phase-randomization proposed by Prichard and Theiler (76) to whole-brain connectomes by extracting the Eigenvectors of the EEG connectome at each sliding window. Subsequently each Eigenvector was Fourier transformed and the phases of this transformation were then randomly shifted. The result of the phase-shift then was back-transformed using the inverse Fourier transform, and the phase shifted Eigenvectors were used to reverse the Eigen-decomposition. This approach has been shown to generate pseudo-connectomes uncorrelated to the original matrix while keeping a similar spatial structure (such as interhemispheric connections and ordering in ICN-like networks) and constant global mean comparable to the original connectome (44)(Fig. 1b).

An explicit test for dynamics is not needed as spurious dynamics are implicitly excluded by combining the two modalities: in the scenario that the previously established static link across the modalities (8) is driving a window-wise constant connectivity in both modalities the entropy of the cross-modal relation - dominated by random noise – would be low, resulting in spurious mutual information close to zero. Spurious dynamics in one modality resulting e.g. from physiological artifacts or sampling error are unlikely to co-occur in the other modality. Exceptions, such as head motion that may affect both modalities at the same time, likely have a spatially distributed impact on many connections of the connectome, and are controlled for by our null model that would preserve such “mass” connectivity changes. The randomization process was carried out 50 times for the EEG connectome, and mutual information to the unaltered fMRI connectome was calculated for each iteration. For final statistical comparison of this null model to the original EEG-fMRI mutual information, we calculated an average mutual information matrix from the 50 iterations for each subject.

To assess the connected set with the strongest EEG-fMRI relationship in each EEG frequency band, we additionally subjected the connection-wise tests against the null model to Network Based Statistics (NBS https://sites.google.com/site/bctnet/comparison/nbs, Version 1.2, correcting for multiple comparisons; (45)). NBS controls the family-wise error rate of the mass-univariate testing at every connection. This method is a non-parametric cluster-based approach to finding connected sets of nodes that significantly differ across thresholded connectivity matrices.

Frequency specific analysis

To test for frequency specificity, we included frequency-specific mutual information matrices of all bands (δEEG-fMRI, θEEG-fMRI, etc.) and for all subjects in an ANOVA (frequency band as 1 factor with 5 levels), while discarding the pseudo-matrices generated for the first statistical analysis. Using NBS an F-Test was carried out to determine if the EEG-bands contributed differentially to the mutual information with fMRI-derived dFC. Posthoc t-tests between one band vs. all the other bands were carried out to explore if any EEG band expressed a network of stronger mutual information than observed in the other bands.

Intrinsic network analysis

To further interpret outcomes in the context of neurocognitive networks, we mapped the extracted 200 connections to 7 canonical intrinsic networks (Visual, Somato-Motor, Default Mode, Fronto-Parietal, Ventral Attention (largely corresponding to Cingulo-opercular (Dosenbach et al. 2006)), Dorsal Attention and Limbic) as described in Yeo et al. (11). The number of connections falling into each network pair were counted (e.g. DMN to Visual). To assure that the observed connectivity pattern did not arise from random sampling into the different networks, we also created 100,000 random

bioRxiv preprint doi: https://doi.org/10.1101/464438; this version posted November 7, 2018. The copyright holder for this preprint (which was not certified by peer review) is the author/funder. All rights reserved. No reuse allowed without permission.

networks of 200 connections to derive the probability that a connection randomly falls into one of the network pairs.

Generalization dataset

Subjects

This dataset comprises 17 healthy adults. Ethical approval has been obtained from the UCL Research Ethics Committee (project ID:4290/001) and informed consent has been obtained from all subjects. One subject was excluded as T1 data quality was not sufficient to run the Freesurfer recon-all command, resulting in a final group of 16 subjects (6 females, mean age: 32.41, range 22-53).

Data Acquisition

We used one session of 10 minutes 48 seconds eyes-open resting-state (Avanto 1.5T, Siemens, 30 slices, TR=2.16s, slice thickness 3mm + 1mm gap, effective voxels size 3.3x3.3x4.0mm, TE = 30ms, field of view 210, flip angle 75 degrees) concurrent EEG-fMRI (63 scalp electrodes BrainCap MR, referenced to FCz, 1 electrode ECG). Scanner clock was timelocked with the MR-compatible amplifier (BrainAmp MR, sampling rate 1kHz) clock . A T1-weighted structural image was also obtained (176 slices, 1.0x1.0x1.0 mm, field of view 256, TR=11min). During the resting-state run, the subjects had their eyes open and were asked to remain awake and fixate on a white cross presented on a black background. Their head was immobilized using a vacuum cushion during scanning.

Data processing

The fMRI data was processed as described for the primary dataset with the exception that no slice-time correction was carried out (in accordance with the original processing in Deligianni (3)). EEG was corrected for the gradient artefact using the template subtraction and adaptive noise cancelation followed by a downsampling to 250Hz and cardiobalistic artefact template subtraction using the Brain Vision Analyzer 2 software (Brain Products, Gilching, Germany). Due to apparent low frequency drift artefacts in several subjects, EEG data was high pass filtered at 0.05Hz instead of the 0.03Hz used in the primary dataset. Because of the differing TR the sliding window for 1 minute was now consisting of 28 volumes (28*2.16s = 60.48s). EEG data processing was equivalent to the primary dataset, with the epochs being 2.16s instead of 2s to match the fMRI TR.

All following analysis steps were identical to the primary dataset.

Acknowledgements

We thank Katia Lehongre and Benjamin Morillon (primary dataset) and Fani Deligianni and Jonathan Clayden (generalization dataset) for generously sharing their data. JW and SS were supported by a Beckman Institute MoCC seed grant. ALG was supported by ERC 260347 – COMPUSLANG.

bioRxiv preprint doi: https://doi.org/10.1101/464438; this version posted November 7, 2018. The copyright holder for this preprint (which was not certified by peer review) is the author/funder. All rights reserved. No reuse allowed without permission.

References

1. Biswal B, Yetkin FZ, Haughton VM, Hyde JS (1995) Functional connectivity in the motor cortex of resting human brain using echo-planar MRI. *Magn Reson Med* 34(4):537–541.

2. Brookes MJ, et al. (2011) Investigating the electrophysiological basis of resting state networks using magnetoencephalography. *PNAS* 108(40):16783–16788.

3. Deligianni F, Centeno M, Carmichael DW, Clayden JD (2014) Relating resting-state fMRI and EEG whole-brain connectomes across frequency bands. *Front Neurosci* 8:258.

4. He BJ, Snyder AZ, Zempel JM, Smyth MD, Raichle ME (2008) Electrophysiological correlates of the brain's intrinsic large-scale functional architecture. *PNAS* 105(41):16039–16044.

5. Hipp JF, Siegel M (2015) BOLD fMRI Correlation Reflects Frequency-Specific Neuronal Correlation. *Current Biology* 25(10):1368–1374.

6. Kucyi A, et al. (2018) Intracranial Electrophysiology Reveals Reproducible Intrinsic Functional Connectivity within Human Brain Networks. *J Neurosci* 38(17):4230–4242.

7. Logothetis NK, Pauls J, Augath M, Trinath T, Oeltermann A (2001) Neurophysiological investigation of the basis of the fMRI signal. *Nature* 412(6843):150–157.

8. Wirsich J, et al. (2017) Complementary contributions of concurrent EEG and fMRI connectivity for predicting structural connectivity. *Neuroimage* 161:251–260.

9. Damoiseaux JS, et al. (2006) Consistent resting-state networks across healthy subjects. *Proc Natl Acad Sci USA* 103(37):13848–13853.

10. Fox MD, et al. (2005) The human brain is intrinsically organized into dynamic, anticorrelated functional networks. *PNAS* 102(27):9673–9678.

11. Yeo BTT, et al. (2011) The organization of the human cerebral cortex estimated by intrinsic functional connectivity. *Journal of Neurophysiology* 106(3):1125–1165.

12. Sporns O, Tononi G, Kötter R (2005) The Human Connectome: A Structural Description of the Human Brain. *PLOS Comput Biol* 1(4):e42.

13. van den Heuvel MP, Hulshoff Pol HE (2010) Exploring the brain network: A review on resting-state fMRI functional connectivity. *European Neuropsychopharmacology* 20(8):519–534.

14. Chang C, Glover GH (2010) Time-frequency dynamics of resting-state brain connectivity measured with fMRI. *Neuroimage* 50(1):81–98.

15. Zalesky A, Fornito A, Cocchi L, Gollo LL, Breakspear M (2014) Time-resolved resting-state brain networks. *PNAS* 111(28):10341–10346.

16. Allen EA, et al. (2014) Tracking Whole-Brain Connectivity Dynamics in the Resting State. *Cereb Cortex* 24(3):663–676.

17. Hansen ECA, Battaglia D, Spiegler A, Deco G, Jirsa VK (2015) Functional connectivity dynamics: Modeling the switching behavior of the resting state. *NeuroImage* 105:525–535.

bioRxiv preprint doi: https://doi.org/10.1101/464438; this version posted November 7, 2018. The copyright holder for this preprint (which was not certified by peer review) is the author/funder. All rights reserved. No reuse allowed without permission.

18. Sadaghiani S, Poline J-B, Kleinschmidt A, D'Esposito M (2015) Ongoing dynamics in large-scale functional connectivity predict perception. *Proc Natl Acad Sci USA* 112(27):8463–8468.

19. Shine JM, et al. (2016) The Dynamics of Functional Brain Networks: Integrated Network States during Cognitive Task Performance. *Neuron* 92(2):544–554.

20. Gratton C, Laumann TO, Gordon EM, Adeyemo B, Petersen SE (2016) Evidence for Two Independent Factors that Modify Brain Networks to Meet Task Goals. *Cell Reports* 17(5):1276–1288.

21. Preti MG, Bolton TA, Van De Ville D (2017) The dynamic functional connectome: State-of-the-art and perspectives. *NeuroImage* 160:41–54.

22. Hindriks R, et al. (2016) Can sliding-window correlations reveal dynamic functional connectivity in resting-state fMRI? *NeuroImage* 127:242–256.

23. Laumann TO, et al. (2017) On the Stability of BOLD fMRI Correlations. *Cereb Cortex* 27(10):4719–4732.

24. Leonardi N, Van De Ville D (2015) On spurious and real fluctuations of dynamic functional connectivity during rest. *Neuroimage* 104:430–436.

25. Singer W (2013) Cortical dynamics revisited. *Trends Cogn Sci (Regul Ed)* 17(12):616–626.

26. Varela F, Lachaux J-P, Rodriguez E, Martinerie J (2001) The brainweb: Phase synchronization and large-scale integration. *Nature Reviews Neuroscience* 2(4):229–239.

27. Sadaghiani S, et al. (2012) Alpha-Band Phase Synchrony Is Related to Activity in the Fronto-Parietal Adaptive Control Network. *J Neurosci* 32(41):14305–14310.

28. Jann K, et al. (2009) BOLD correlates of EEG alpha phase-locking and the fMRI default mode network. *Neuroimage* 45(3):903–916.

29. Hassan M, Wendling F (2018) Electroencephalography Source Connectivity: Aiming for High Resolution of Brain Networks in Time and Space. *IEEE Signal Processing Magazine* 35(3):81–96.

30. O'Neill GC, et al. (2018) Dynamics of large-scale electrophysiological networks: A technical review. *NeuroImage* 180:559–576.

31. de Pasquale F, et al. (2010) Temporal dynamics of spontaneous MEG activity in brain networks. *Proc Natl Acad Sci USA* 107(13):6040–6045.

32. Vidaurre D, et al. (2018) Spontaneous cortical activity transiently organises into frequency specific phase-coupling networks. *Nature Communications* 9(1):2987.

33. Chang C, Liu Z, Chen MC, Liu X, Duyn JH (2013) EEG correlates of time-varying BOLD functional connectivity. *Neuroimage* 72:227–236.

34. Tagliazucchi E, Von Wegner F, Morzelewski A, Brodbeck V, Laufs H (2012) Dynamic BOLD functional connectivity in humans and its electrophysiological correlates. *Front Hum Neurosci* 6:339.

35. Allen EA, Damaraju E, Eichele T, Wu L, Calhoun VD (2017) EEG Signatures of Dynamic Functional Network Connectivity States. *Brain Topogr*:1–16.

bioRxiv preprint doi: https://doi.org/10.1101/464438; this version posted November 7, 2018. The copyright holder for this preprint (which was not certified by peer review) is the author/funder. All rights reserved. No reuse allowed without permission.

36. Thompson GJ (2018) Neural and metabolic basis of dynamic resting state fMRI. *NeuroImage* 180:448–462.

37. Thompson GJ, et al. (2013) Neural correlates of time-varying functional connectivity in the rat. *NeuroImage* 83:826–836.

38. Ridley B, et al. (2017) Simultaneous Intracranial EEG-fMRI Shows Inter-Modality Correlation in Time-Resolved Connectivity Within Normal Areas but Not Within Epileptic Regions. *Brain Topogr* 30(5):639–655.

39. Desikan RS, et al. (2006) An automated labeling system for subdividing the human cerebral cortex on MRI scans into gyral based regions of interest. *Neuroimage* 31(3):968–980.

40. Fischl B, et al. (2004) Automatically parcellating the human cerebral cortex. *Cereb Cortex* 14(1):11–22.

41. Baillet S, Mosher JC, Leahy RM (2001) Electromagnetic brain mapping. *IEEE Signal Processing Magazine* 18(6):14–30.

42. Kybic J, et al. (2005) A common formalism for the Integral formulations of the forward EEG problem. *IEEE Transactions on Medical Imaging* 24(1):12–28.

43. Tadel F, Baillet S, Mosher JC, Pantazis D, Leahy RM (2011) Brainstorm: A User-Friendly Application for MEG/EEG Analysis. *Comput Intell Neurosci* 2011. doi:10.1155/2011/879716.

44. Tewarie P, et al. (2016) Predicting haemodynamic networks using electrophysiology: The role of non-linear and cross-frequency interactions. *NeuroImage* 130:273–292.

45. Zalesky A, et al. (2010) Whole-brain anatomical networks: Does the choice of nodes matter? *NeuroImage* 50(3):970–983.

46. Power JD, Plitt M, Laumann TO, Martin A (2017) Sources and implications of whole-brain fMRI signals in humans. *NeuroImage* 146:609–625.

47. Britz J, Van De Ville D, Michel CM (2010) BOLD correlates of EEG topography reveal rapid resting-state network dynamics. *Neuroimage* 52(4):1162–1170.

48. Hunyadi B, Woolrich M, Quinn A, Vidaurre D, De Vos M (2018) A dynamic system of brain networks revealed by fast transient EEG fluctuations and their fMRI correlates. *NeuroImage*. doi:10.1016/j.neuroimage.2018.09.082.

49. Hiltunen T, et al. (2014) Infra-Slow EEG Fluctuations Are Correlated with Resting-State Network Dynamics in fMRI. *J Neurosci* 34(2):356–362.

50. Leistner S, et al. (2010) Magnetoencephalography discriminates modality-specific infraslow signals less than 0.1 Hz. *Neuroreport* 21(3):196–200.

51. de Pasquale F, et al. (2012) A Cortical Core for Dynamic Integration of Functional Networks in the Resting Human Brain. *Neuron* 74(4):753–764.

52. Margulies DS, et al. (2016) Situating the default-mode network along a principal gradient of macroscale cortical organization. *PNAS* 113(44):12574–12579.

53. Laufs H, et al. (2003) EEG-correlated fMRI of human alpha activity. *Neuroimage* 19(4):1463–1476.

bioRxiv preprint doi: https://doi.org/10.1101/464438; this version posted November 7, 2018. The copyright holder for this preprint (which was not certified by peer review) is the author/funder. All rights reserved. No reuse allowed without permission.

54. Sadaghiani S, et al. (2010) Intrinsic connectivity networks, alpha oscillations, and tonic alertness: a simultaneous electroencephalography/functional magnetic resonance imaging study. *J Neurosci* 30(30):10243–10250.

55. Farahibozorg S-R, Henson RN, Hauk O (2018) Adaptive cortical parcellations for source reconstructed EEG/MEG connectomes. *NeuroImage* 169:23–45.

56. Iannotti GR, Pittau F, Michel CM, Vulliemoz S, Grouiller F (2015) Pulse Artifact Detection in Simultaneous EEG–fMRI Recording Based on EEG Map Topography. *Brain Topogr* 28(1):21–32.

57. Hedrich T, Pellegrino G, Kobayashi E, Lina JM, Grova C (2017) Comparison of the spatial resolution of source imaging techniques in high-density EEG and MEG. *NeuroImage* 157:531–544.

58. Hacker CD, Snyder AZ, Pahwa M, Corbetta M, Leuthardt EC (2017) Frequency-specific electrophysiologic correlates of resting state fMRI networks. *Neuroimage* 149:446–457.

59. Lu H, et al. (2007) Synchronized delta oscillations correlate with the resting-state functional MRI signal. *Proc Natl Acad Sci U S A* 104(46):18265–18269.

60. Pan W-J, et al. (2011) Broadband Local Field Potentials Correlate with Spontaneous Fluctuations in Functional Magnetic Resonance Imaging Signals in the Rat Somatosensory Cortex Under Isoflurane Anesthesia. *Brain Connectivity* 1(2):119–131.

61. Deligianni F, Carmichael DW, Zhang GH, Clark CA, Clayden JD (2016) NODDI and Tensor-Based Microstructural Indices as Predictors of Functional Connectivity. *PLOS ONE* 11(4):e0153404.

62. Mandelkow H, Halder P, Boesiger P, Brandeis D (2006) Synchronization facilitates removal of MRI artefacts from concurrent EEG recordings and increases usable bandwidth. *NeuroImage* 32(3):1120–1126.

63. Morillon B, et al. (2010) Neurophysiological origin of human brain asymmetry for speech and language. *PNAS* 107(43):18688–18693.

64. Power JD, et al. (2014) Methods to detect, characterize, and remove motion artifact in resting state fMRI. *Neuroimage* 84:320–341.

65. Allen PJ, Josephs O, Turner R (2000) A method for removing imaging artifact from continuous EEG recorded during functional MRI. *Neuroimage* 12(2):230–239.

66. Allen PJ, Polizzi G, Krakow K, Fish DR, Lemieux L (1998) Identification of EEG events in the MR scanner: the problem of pulse artifact and a method for its subtraction. *Neuroimage* 8(3):229–239.

67. Gramfort A, Papadopoulo T, Olivi E, Clerc M (2010) OpenMEEG: opensource software for quasistatic bioelectromagnetics. *BioMedical Engineering OnLine* 9:45.

68. Nolte G, et al. (2004) Identifying true brain interaction from EEG data using the imaginary part of coherency. *Clin Neurophysiol* 115(10):2292–2307.

69. Power JD, Barnes KA, Snyder AZ, Schlaggar BL, Petersen SE (2012) Spurious but systematic correlations in functional connectivity MRI networks arise from subject motion. *NeuroImage* 59(3):2142–2154.

bioRxiv preprint doi: https://doi.org/10.1101/464438; this version posted November 7, 2018. The copyright holder for this preprint (which was not certified by peer review) is the author/funder. All rights reserved. No reuse allowed without permission.

70. Shirer WR, Ryali S, Rykhlevskaia E, Menon V, Greicius MD (2012) Decoding Subject-Driven Cognitive States with Whole-Brain Connectivity Patterns. *Cereb Cortex* 22(1):158–165.

71. Zalesky A, Breakspear M (2015) Towards a statistical test for functional connectivity dynamics. *Neuroimage* 114:466–470.

72. Studholme C, Hawkes DJ, Hill DLG (1998) Normalized entropy measure for multimodality image alignment. *Medical Imaging 1998: Image Processing* (International Society for Optics and Photonics), pp 132–144.

73. Studholme C, Hill DL, Hawkes DJ (1997) Automated three-dimensional registration of magnetic resonance and positron emission tomography brain images by multiresolution optimization of voxel similarity measures. *Med Phys* 24(1):25–35.

74. Shannon CE (1948) A Mathematical Theory of Communication. *Bell System Technical Journal* 27(3):379–423.

75. Ostwald D, Porcaro C, Bagshaw AP (2010) An information theoretic approach to EEG-fMRI integration of visually evoked responses. *Neuroimage* 49(1):498–516.

76. Prichard D, Theiler J (1994) Generating surrogate data for time series with several simultaneously measured variables. *Phys Rev Lett* 73(7):951–954.

bioRxiv preprint doi: https://doi.org/10.1101/464438; this version posted November 7, 2018. The copyright holder for this preprint (which was not certified by peer review) is the author/funder. All rights reserved. No reuse allowed without permission.

Supplementary Information

SI: Results

Mutual information strength

The top-200 connections (Fig. 4) were selected by the difference in mutual information magnitude compared to the null model. It remains unclear whether the average mutual information of the top-200 connections was higher in the significant connection cluster selected by NBS compared to non-selected values. Indeed, across both datasets and for all EEG bands, we found stronger mutual information within the top-200 compared to non-selected connections (one sided t-test, main data; fMRI vs. δ/θ/α/β/γ: $p=8.57*10^{-23}/3.17*10^{-15}/2.25*10^{-14}/3.61*10^{-18}/8.20*10^{-16}$, generalization data; fMRI vs. δ/θ/α/β/γ: $p=2.95*10^{-14}/2.49*10^{-26}/1.46*10^{-18}/4.35*10^{-9}/4.72*10^{-16}$, $p<0.05$).

We further confirmed that the MI magnitude difference between the top 200 connections and the rest of the connections is consistent across the two datasets. We performed an analogous test between the two datasets by masking the generalization data with the top-200 connections of the main dataset. MI was generally increased as compared to the rest of the connections for MI between fMRI and δ/θ/α but not increased for MI between fMRI and β/γ (one-sided ttest, fMRI vs. δ/θ/α/β/γ: $p=5.00*10^{-7}/3.71*10^{-8}/0.012/0.053/0.428$, $p<0.05$).

When assessing generalization at a connection-wise resolution, we observed correlation of connection-wise EEG-fMRI mutual information for δ, θ, and α bands but not for β and γEEG (Fig. 3). To assess whether this discrepancy was due to lower signal to noise ratio in the higher frequencies, we investigated whether replication *within* each dataset would show a similar pattern. We divided the primary dataset (respectively the generalization dataset) into two groups of 8 subjects each (taking only the first 16 subjects of the primary dataset). Indeed, we observed a within dataset correlation of fMRI vs. δ/θ/α connection-wise mutual information, whereas no correlation between fMRI vs. β/γ was observed (Table S1).

Table S1: Within group correlation of mutual information when splitting up the subjects into two groups of 8 (for main dataset the first 16 subjects were taken to create equal groups of 8)

	Delta-fMRI	Theta-fMRI	Alpha-fMRI	Beta-fMRI	Gamma-fMRI
Main dataset	0.43	0.27	0.17	0.03	0.03
Generalization Data	0.36	0.29	0.21	0.04	0.001

Mutual information strength of frequency specific networks

Within the subnetworks selected by NBS (Fig. 5), we further tested for connection-wise correlation of mutual information strength between the two datasets. When masked by the top-100 connections of the 'δ > other bands' contrast of the main dataset (Table 2), the correlation between mutual information (averaged across all subjects) across the two datasets was: $r=0.56$ ($p=2.0*10^{-9}$), a value qualitatively higher than for the whole brain ($r=0.48$). Contrarily, masking the top-100 connections of the 'γ > other bands' contrast $r=-0.0785$ was not significant ($p=0.44$, in line with the missing relationship between connection-wise MI correlation in gamma; Fig. 3).

When counting the number of the top-100 significant connections over the seven canonical networks, the count of delta and gamma networks were correlated across datasets: δEEG-fMRI/γEEG-fMRI: $r=0.90/0.68$, $p=2.9*10^{-8}/6.1*10^{-4}$.

bioRxiv preprint doi: https://doi.org/10.1101/464438; this version posted November 7, 2018. The copyright holder for this preprint (which was not certified by peer review) is the author/funder. All rights reserved. No reuse allowed without permission.

Generalization of MI distribution across canonical intrinsic networks

We established that this distribution of the top 200 connections and the ensuing DMN-dominance were not driven by the number of ICN nodes or other potential biases. For each network pair (e.g. DMN-VIS) we tested whether the number of connections was significantly higher than chance by randomly selecting (n=100,000 iterations) 200 connections from the main dataset (Table S2-S6).

Table S2: p-values of comparing the number of top-200 most significant δEEG-fMRI connections falling within an ICN-ICN pair as compared to randomly sampling 200 connections of the brain (100.000 iterations); significant connections are highlighted in green and yellow p<0.0018 (p<0.05, Bonferroni corrected for 28 connections, yellow cell did not replicate at uncorrected threshold p<0.05 in generalization dataset).

	VIS	SM	DA	VA	L	FP	DMN
VIS	0,0399	0,0425	0,5069	0,9526	0,0123	0,0011	0,0004
SM		0,2022	0,1143	0,1068	0,0099	0,5647	0,0008
DA			1	0,1133	0,0511	0,0269	0,1208
VA				1	0,0647	0,1137	0,0008
L					0,7785	0,3319	0,0004
FP						1	0,0059
DMN							0,0003

Table S3: p-values of comparing the number of top-200 most significant ϑEEG-fMRI connections falling within an ICN-ICN pair as compared to randomly sampling 200 connections of the brain (100.000 iterations); significant connections are highlighted in green p<0.0018 (p<0.05, Bonferroni corrected for 28 connections).

	VIS	SM	DA	VA	L	FP	DMN
VIS	0,2969	0,1826	0,5129	0,0086	0,1349	0,0062	0
SM		0,008	0,0375	0	0,1943	0,0098	0,0022
DA			1	0,0291	0,1449	0,1434	0,0506
VA				0,0567	0,6972	0,7022	0,0009
L					0,9436	0,6114	0,0248
FP						0,0238	0,0186
DMN							0,0136

Table S4: p-values of comparing the number of 200 most significant αEEG-fMRI connections falling within an ICN-ICN pair as compared to randomly sampling 200 connections of the brain (100.000 iterations); significant connections are highlighted in green p<0.0018 (p<0.05, Bonferroni corrected for 28 connections).

	VIS	SM	DA	VA	L	FP	DMN
VIS	0,1209	0,017	0,0874	0,1725	0,2431	0,0886	0,0018
SM		0,0279	0,284	0,0012	0,1955	0,0021	0
DA			1	0,3326	0,6106	0,0039	0,0019
VA				1	0,6957	1	0,0149
L					0,9431	0,3327	0,0821
FP						1	0,0506
DMN							0

Table S5: p-values of comparing the number of top-200 most significant βEEG-fMRI connections falling within an ICN-ICN pair as compared to randomly sampling 200 connections of the brain (100.000 iterations); significant connections are highlighted in green and yellow p<0.0018 (p<0.05, Bonferroni corrected for 28 connections, yellow cell did not replicate at uncorrected threshold p<0.05 in generalization dataset).

	VIS	SM	DA	VA	L	FP	DMN
VIS	0,1202	0,5011	0,8227	0,9518	0,3994	0,5101	0,0003
SM		0,415	0,5629	0,4113	0,0036	0,2875	0,0001

bioRxiv preprint doi: https://doi.org/10.1101/464438; this version posted November 7, 2018. The copyright holder for this preprint (which was not certified by peer review) is the author/funder. All rights reserved. No reuse allowed without permission.

DA			1	0,1128	0,0149	0,1477	0,0514
VA				1	0,1428	0,7049	0,0725
L					0,5344	0,1485	0
FP						0,0013	0,0527
DMN							0

Table S6: p-values of comparing the number of top-200 most significant γEEG-fMRI connections falling within an ICN-ICN pair as compared to randomly sampling 200 connections of the brain (100.000 iterations); significant connections are highlighted in green and yellow p<0.0018 (p<0.05, Bonferroni corrected for 28 connections, yellow cell did not replicate at uncorrected threshold p<0.05 in generalization dataset).

	VIS	SM	DA	VA	L	FP	DMN
VIS	0,0393	0,1826	0,5118	0,027	0,012	0,0861	0,0018
SM		0,0276	0,5603	0,4127	0,0237	0,5622	0,0001
DA			1	0,1128	0,6088	1	0,6656
VA				0,2241	0,0002	0,3323	0
L					0,1455	0,61	0,0001
FP						1	0,2511
DMN							0,0025

Atlas and ICN labels

Table S7: Regions of the Desikan atlas (39) and their mapping to the canonical ICN networks (11)

	Region name	Short name	ICN
1	left cuneus	lCUN	Visual
2	left fusiform	lFUS	Visual
3	left lateraloccipital	lLOG	Visual
4	left lingual	lLING	Visual
5	left pericalcarine	lperiCAL	Visual
6	right cuneus	rCUN	Visual
7	right fusiform	rFUS	Visual
8	right lateraloccipital	rLOG	Visual
9	right lingual	rLING	Visual
10	right pericalcarine	rperiCAL	Visual
11	left paracentral	lparaC	Somato Motor
12	left postcentral	lpostC	Somato Motor
13	left precentral	lpreC	Somato Motor
14	left superiortemporal	lSTG	Somato Motor
15	left transversetemporal	lTT	Somato Motor
16	right paracentral	rparaC	Somato Motor
17	right postcentral	rpostC	Somato Motor
18	right posteriorcingulate	rPCC	Somato Motor
19	right precentral	rpreC	Somato Motor
20	right superiortemporal	rSTG	Somato Motor
21	right transversetemporal	rTT	Somato Motor
22	left caudalmiddlefrontal	lcMFG	Dorsal Attention
23	left superiorparietal	lSPL	Dorsal Attention
24	right caudalmiddlefrontal	rcMFG	Dorsal Attention
25	right superiorparietal	rSPL	Dorsal Attention
26	left caudalanteriorcingulate	lcACC	Ventral Attention

bioRxiv preprint doi: https://doi.org/10.1101/464438; this version posted November 7, 2018. The copyright holder for this preprint (which was not certified by peer review) is the author/funder. All rights reserved. No reuse allowed without permission.

27	left parsopercularis	lpOPER	Ventral Attention
28	left supramarginal	lSMAR	Ventral Attention
29	left insula	lINS	Ventral Attention
30	right caudalanteriorcingulate	rcACC	Ventral Attention
31	right supramarginal	rSMAR	Ventral Attention
32	right insula	rINS	Ventral Attention
33	left entorhinal	lENT	Limbic
34	left inferiortemporal	lITG	Limbic
35	left lateralorbitofrontal	lLOF	Limbic
36	left medialorbitofrontal	lMOF	Limbic
37	left frontalpole	lFP	Limbic
38	left temporalpole	lTP	Limbic
39	right entorhinal	rENT	Limbic
40	right inferiortemporal	rITG	Limbic
41	right lateralorbitofrontal	rLOF	Limbic
42	right medialorbitofrontal	rMOF	Limbic
43	right frontalpole	rFP	Limbic
44	right temporalpole	rTP	Limbic
45	left rostralmiddlefrontal	lrMFG	Fronto Parietal
46	right parsopercularis	rpOPER	Fronto Parietal
47	right parstriangularis	rpTRI	Fronto Parietal
48	right rostralmiddlefrontal	rrMFG	Fronto Parietal
49	left bankssts	lBSTS	Default Mode
50	left inferiorparietal	lIPL	Default Mode
51	left isthmuscingulate	liCC	Default Mode
52	left middletemporal	lMTG	Default Mode
53	left parsorbitalis	lpORB	Default Mode
54	left parstriangularis	lpTRI	Default Mode
55	left posteriorcingulate	lPCC	Default Mode
56	left precuneus	lPCUN	Default Mode
57	left rostralanteriorcingulate	lrACC	Default Mode
58	left superiorfrontal	lSFG	Default Mode
59	right bankssts	rBSTS	Default Mode
60	right inferiorparietal	rIPL	Default Mode
61	right isthmuscingulate	riCC	Default Mode
62	right middletemporal	rMTG	Default Mode
63	right parsorbitalis	rpORB	Default Mode
64	right precuneus	rPCUN	Default Mode
65	right rostralanteriorcingulate	rrACC	Default Mode
66	right superiorfrontal	rSFG	Default Mode
67	left parahippocampal	lPARH	Default Mode
68	right parahippocampal	rPARH	Default Mode